Dynamics and dissipation in enzyme catalysis

Nicholas Boekelheide, Romelia Salomón-Ferrer, and Thomas F. Miller III[1]

Division of Chemistry and Chemical Engineering, California Institute of Technology, 1200 East California Boulevard, Mail Code 127-72, Pasadena, CA 91125

Edited by Donald G. Truhlar, University of Minnesota, Minneapolis, MN, and approved August 5, 2011 (received for review April 21, 2011)

We use quantized molecular dynamics simulations to characterize the role of enzyme vibrations in facilitating dihydrofolate reductase hydride transfer. By sampling the full ensemble of reactive trajectories, we are able to quantify and distinguish between statistical and dynamical correlations in the enzyme motion. We demonstrate the existence of nonequilibrium dynamical coupling between protein residues and the hydride tunneling reaction, and we characterize the spatial and temporal extent of these dynamical effects. Unlike statistical correlations, which give rise to nanometer-scale coupling between distal protein residues and the intrinsic reaction, dynamical correlations vanish at distances beyond 4–6 Å from the transferring hydride. This work finds a minimal role for nonlocal vibrational dynamics in enzyme catalysis, and it supports a model in which nanometer-scale protein fluctuations statistically modulate—or gate—the barrier for the intrinsic reaction.

enzyme dynamics | hydrogen tunneling | path integral | ring polymer molecular dynamics

Protein motions are central to enzyme catalysis, with conformational changes on the micro- and millisecond timescale well-established to govern progress along the catalytic cycle (1, 2). Less is known about the role of faster, atomic-scale fluctuations that occur in the protein environment of the active site. The textbook view of enzyme-catalyzed reaction mechanisms neglects the functional role of such fluctuations and describes a static protein environment that both scaffolds the active-site region and reduces the reaction barrier (3). This view has grown controversial amid evidence that active-site chemistry is coupled to motions in the enzyme (4–6), and it has been explicitly challenged by recent proposals that enzyme-catalyzed reactions are driven by vibrational excitations that channel energy into the intrinsic reaction coordinate (7, 8) or promote reactive tunneling (9, 10). In the following, we combine quantized molecular dynamics and rare-event sampling methods to determine the mechanism by which protein motions couple to reactive tunneling in dihydrofolate reductase and to clarify the role of nonequilibrium vibrational dynamics in enzyme catalysis.

Manifestations of enzyme motion include both statistical and dynamical correlations. Statistical correlations are properties of the equilibrium ensemble and describe, for example, the degree to which fluctuations in the spatial position of one atom are influenced by fluctuations in another; these correlations govern the free-energy (FE) landscape and determine the transition state theory kinetics of the system (6). Dynamical correlations are properties of the time-evolution of the system and describe coupling between inertial atomic motions, as in a collective vibrational mode. Compelling evidence for long-ranged (i.e., nanometer-scale) networks of statistical correlations in enzymes emerges from genomic analysis (11), molecular dynamics simulations (11–13), and kinetic studies of double-mutant enzymes (14–16). But the role of dynamical correlations in enzyme catalysis remains unresolved (4, 5, 7, 17, 18), with experimental and theoretical results suggesting that the intrinsic reaction is activated by vibrational modes involving the enzyme active site (9, 19, 20) and more distant protein residues (7, 8, 21). The degree to which enzyme-catalyzed reactions are coupled to the surrounding protein environment, and the lengthscales and timescales over which such couplings persist, are central questions in the understanding, regulation, and de novo design of biological catalysts (22).

Escherichia coli dihydrofolate reductase (DHFR) is an extensively studied prototype for protein motions in enzyme catalysis. It catalyzes reduction of the 7,8-dihydrofolate (DHF) substrate via hydride transfer from the nicotinamide adenine dinucleotide phosphate (NADPH) cofactor (Fig. 1*A* and Fig. S1). We investigate this intrinsic reaction using ring polymer molecular dynamics (RPMD) (23, 24), a recently developed path-integral method that enables inclusion of nuclear quantization effects, such as the zero-point energy and tunneling, in the dynamics of the transferring hydride. RPMD simulations with over 14,000 atoms are performed using explicit solvent and using an empirical valence bond (EVB) potential to describe the potential energy surface for the transferring hydride; the EVB potential is obtained from an effective Hamiltonian matrix, with diagonal elements ($V_{\mathrm{r}}(\mathbf{x})$ and $V_{\mathrm{p}}(\mathbf{x})$) corresponding to the potential energy for the reactant and product bonding connectivities and with the constant off-diagonal matrix element fit to the experimental rate (11, 25). The vector $\mathbf{x}$ includes the position of the quantized hydride and all classical nuclei in the system. The EVB potential employed here was chosen for consistency with earlier simulation studies of DHFR (11, 26); although the mechanistic issues addressed in this study are not expected to be highly sensitive to the details of the potential energy surface, it should be noted that more accurate electronic structure theory methods for describing the enzyme potential energy surface, including the combined quantum mechanical and classical mechanical (QM/MM) method, are available and widely used in enzyme simulations.

The thermal reaction rate is calculated from the product of the Boltzmann-weighted activation FE and the reaction transmission coefficient (24), both of which are calculated in terms of the dividing surface $\lambda(\mathbf{x}) = -4.8$ kcal/mol where $\lambda(\mathbf{x}) = V_{\mathrm{r}}(\mathbf{x}) - V_{\mathrm{p}}(\mathbf{x})$. The FE surface $F(\lambda)$ is obtained using over 120 ns of RPMD sampling (Fig. 1*B*), and the transmission coefficient is obtained from over 5,000 RPMD trajectories that are released from the Boltzmann distribution constrained to the dividing surface (Fig. 1*C*). In contrast to mixed quantum-classical and transition state theory methods, RPMD yields reaction rates and mechanisms that are formally independent of the choice of dividing surface or any other reaction coordinate assumption (24). Furthermore, the RPMD method enables generation of the ensemble of reactive, quantized molecular dynamics trajectories, which is essential for the following analysis of dynamical correlations. Calculation details, including a description of the rare-event sampling methodology used to generate the unbiased

Author contributions: N.B., R.S.-F., and T.F.M. designed research, performed research, contributed new reagents/analytic tools, analyzed data, and wrote the paper.

The authors declare no conflict of interest.

This article is a PNAS Direct Submission.

Freely available online through the PNAS open access option.

[1]To whom correspondence should be addressed. E-mail: tfm@caltech.edu.

This article contains supporting information online at www.pnas.org/lookup/suppl/doi:10.1073/pnas.1106397108/-/DCSupplemental.

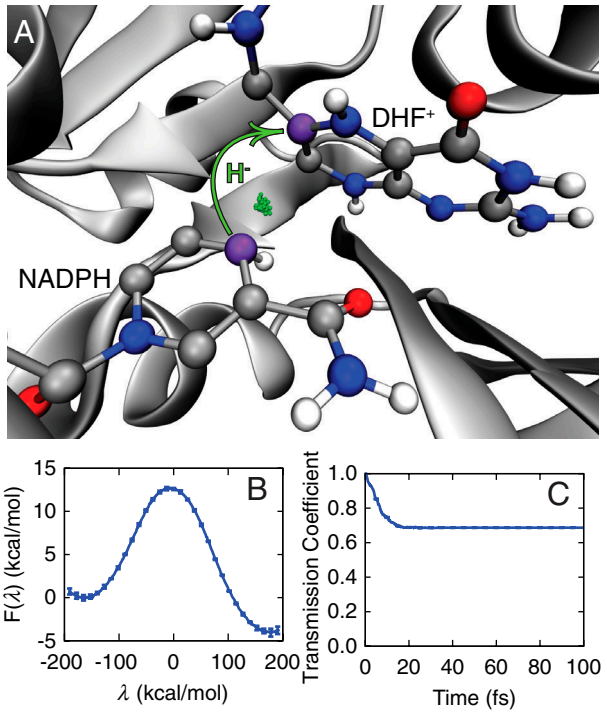

Fig. 1. The hydride transfer reaction catalyzed by DHFR. (*A*) The active site with the hydride (green) shown in the ring-polymer representation of the quantized MD and the donor and acceptor C atoms in purple. (*B*) The quantized free-energy profile for the reaction. (*C*) The time-dependent transmission coefficient corresponding to the dividing surface at $\lambda(\mathbf{x}) = -4.8$ kcal/mol.

ensemble of reactive trajectories (27, 28), are provided in *Materials and Methods* below.

Results and Discussion

The time-dependence of the transmission coefficient in Fig. 1*C* confirms that reactive trajectories commit to the reactant or product basins within 25 fs. The near-unity value of this transmission coefficient at long times indicates that recrossing of the dividing surface in reactive trajectories is a modest effect, although it is fully accounted for in this study, and it confirms that the collective variable $\lambda(\mathbf{x})$ provides a good measure of progress along the intrinsic reaction. We find that quantization of the hydride lowers the FE barrier by approximately 3.5 kcal/mol (Fig. S2), in agreement with earlier work (29, 30).

Statistical correlations among the protein and enzyme active-site coordinates are shown in Fig. 2*A*. The normalized covariance among atom position fluctuations, $c_{ij} = C_{ij}/(C_{ii}C_{jj})^{1/2}$ such that

$$C_{ij} = \langle(\mathbf{x}_i - \langle\mathbf{x}_i\rangle)\cdot(\mathbf{x}_j - \langle\mathbf{x}_j\rangle)\rangle \quad [1]$$

is plotted for the Boltzmann distribution in the reactant, dividing surface, and product regions. The figure shows correlations among the protein α-carbons and the heavy atoms of the substrate and cofactor; the corresponding all-atom correlation plots are provided in Fig. S3. As has been previously and correctly emphasized (11, 29, 30), structural fluctuations in the active-site and distal protein residues are richly correlated within each region, which contributes to nonadditive effects in the kinetics of DHFR mutants (14, 31). Furthermore, the network of correlations varies among the three ensembles, indicating that fluctuations in distal protein residues respond to the adiabatic progress of the hydride from reactant to product. However, these time-averaged quantities do not address the role of dynamical correlations between the transferring hydride and its environment, which depend on the hierarchy of timescales for motion in the system.

To characterize dynamical correlations in the intrinsic reaction, we introduce a measure of velocity cross-correlations in the reactive trajectories, $d_{ij}(t) = D_{ij}(t)/(D_{ii}(t)D_{jj}(t))^{1/2}$ such that

$$D_{ij}(t) = \langle\mathbf{v}_i\cdot\mathbf{v}_j\rangle_t. \quad [2]$$

Here, $\langle\ldots\rangle_t$ denotes an average over the nonequilibrium ensemble of phase-space points that lie on reactive trajectories that crossed the dividing surface some time t earlier and subsequently terminate in the product basin. This quantity, which vanishes for

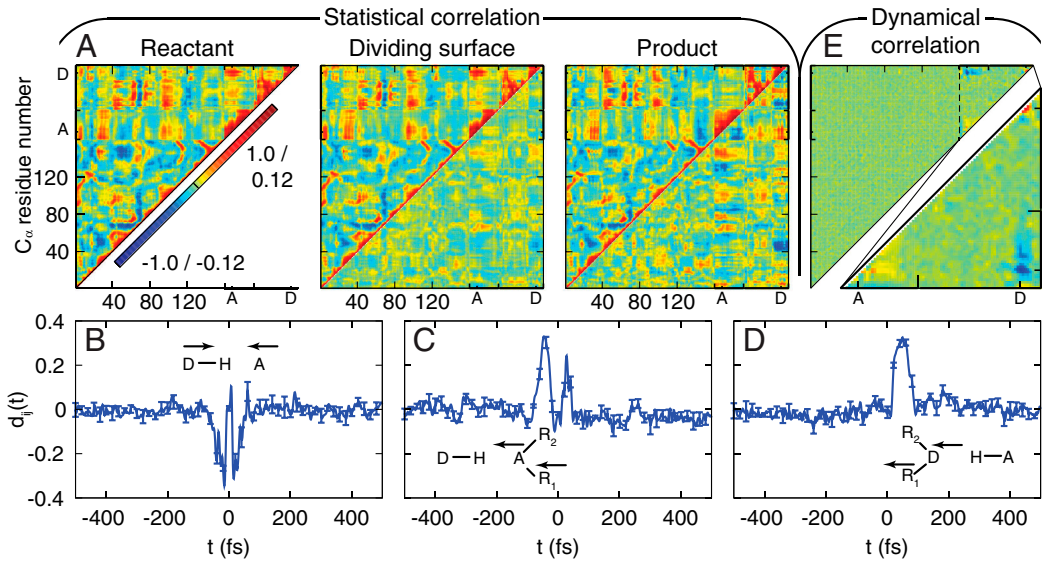

Fig. 2. Statistical and dynamical correlations among enzyme motions during the intrinsic reaction. (*A*) (Upper triangles) The covariance c_{ij} among position fluctuations in DHFR, plotted for the reactant, dividing surface, and product regions. Protein residues are indexed according to [Protein Data Bank (PDB) 1RX2]; substrate and cofactor regions are indicated by the hydride acceptor A and donor D atoms, respectively. (Lower triangles) The difference with respect to the plot for the reactant basin. (*B–D*) The dynamical correlation measure $d_{ij}(t)$ for (*B*) the donor and acceptor atom pair, (*C*) the substrate-based C_7 and acceptor atom pair, and (*D*) the cofactor-based C_{N3} and donor atom pair. Results for additional atom pairs are presented in Fig. S5. (*E*) (Upper triangle) The integrated dynamical correlation measure d_{ij}, indexed as in (*A*). Significant dynamical correlations appear primarily in the substrate and cofactor regions, which are enlarged in the lower triangle.

the equilibrium ensemble, reports on the degree to which atoms move in concert during the intrinsic reaction step. Fig. 2 *B–D* show $d_{ij}(t)$ for several atomic pairs in the active site. Negative dynamical correlations are seen between the donor and acceptor C atoms (Fig. 2*B*), which move in opposite directions (first approaching each other, then moving apart) during the hydride transfer. Similarly, positive correlations are seen between atom pairs on the cofactor (Fig. 2*C*) and on the substrate (Fig. 2*D*) that move in concert as the hydride is transferred. In each case, the primary features of the correlation decay within $\tau = 100$ fs.

Fig. 2*E* summarizes the extent of dynamical correlations throughout the enzyme system in terms of $d_{ij} = \int_{-\tau}^{\tau} d_{ij}(t)dt$. Only atoms in the substrate and cofactor regions (Fig. 2*E*, lower triangle) and a small number of protein atoms in the active-site region exhibit appreciable signal. The same conclusions are reached upon integrating the absolute value of the $d_{ij}(t)$ (Fig. S4), emphasizing that this lack of signal in the protein residues is not simply due to the time integration. Instead, Fig. 2*E* reveals that the dynamical correlations between distal protein residues and the intrinsic reaction do not exist on any timescale. We also provide measures for dynamical correlations that are nonlocal in time (Fig. S5) and for dynamical correlations among perpendicular motions (Fig. S6), but the following conclusion is unchanged. The extensive network of statistical correlations (Fig. 2*A*) is neither indicative of, nor accompanied by, an extensive network of dynamical correlations during the intrinsic reaction (Fig. 2*E*).

A combined measure of the dynamical correlation between a given atom and the intrinsic reaction event can be obtained from the nonequilibrium ensemble average of velocities in the reactive trajectories. Specifically, we consider $f_i^{\xi}(t) = \langle v_i^{\xi} \cdot \Delta\lambda(\mathbf{x})\rangle_t$, where $\xi \in \{x,y,z\}$ indicates the component of the velocity, the filter $\Delta\lambda(\mathbf{x}) = (\bar{\lambda} - |\lambda(\mathbf{x})|)/\bar{\lambda}$ selects configurations in the region of the dividing surface, and $\bar{\lambda} = 177$ kcal/mol is the average magnitude of $\lambda(\mathbf{x})$ in the reactant and product regions. Each component of $\mathbf{f}_i(t)$ vanishes trivially at equilibrium. Fig. 3 *A–C* presents the measure for various atoms in the active-site region. The donor and acceptor C atoms (Fig. 3 *A* and *B*) are both strongly correlated with the dynamics of the intrinsic reaction, whereas the O atom in the Y100 residue of the active site (Fig. 3*C*) reveals smaller, but nonzero, signatures of dynamical correlation. Fig. 3*D* presents $f_i = \int_{-\tau}^{\tau} |\mathbf{f}_i(t)|^2 dt$ for each atom, summarizing the degree to which all atoms in the active site exhibit dynamical correlations, and Fig. 3*E* compares the correlation lengthscales in the enzyme. The main panel in Fig. 3*E* presents f_i as a function of the distance of heavy atoms from the midpoint of the hydride donor and acceptor, and the inset similarly presents the distance dependence of the statistical correlation measure $\bar{c}_i = (c_{i\mu} + c_{i\nu})/2$, where c_{ij} is defined previously and where indices μ and ν label the donor and acceptor carbon atoms, respectively. Whereas the statistical correlations reach the nanometer lengthscale and involve the protein environment, dynamical correlations are extremely local in nature and primarily confined to the enzyme substrate and cofactor.

Fig. 4 illustrates that dynamical correlations in the intrinsic reaction are limited by disparities in the relative timescales for enzyme motion. The figure presents two-dimensional projections of the FE surface, $F(\lambda,\Theta_\alpha)$, where $\alpha \in \{1,2\}$, $\Theta_1(\mathbf{x})$ is the distance between hydride donor and acceptor atoms, and $\Theta_2(\mathbf{x})$ is the separation between active-site protein atoms I14 C_δ and Y100 O (side chain). Overlaid on the surfaces are the minimum FE pathway between the reactant and product basins, s, and the time-parameterized pathway followed by the ensemble of reactive trajectories, $\sigma = (\langle\lambda(\mathbf{x})\rangle_t, \langle\Theta_\alpha(\mathbf{x})\rangle_t)$. Nonzero slope in s indicates statistical correlation of Θ_α with λ, whereas the same feature in σ indicates that the dynamics of Θ_α and λ are dynamically correlated. Fig. 4*A* confirms that the donor-acceptor distance is both statistically and dynamically correlated with the intrinsic reaction. In contrast, Fig. 4*B* reveals significant statistical correlation between Θ_2 and the intrinsic reaction, but the reactive trajectories traverse the dividing surface region on a timescale that is too fast to dynamically couple to the protein coordinate.

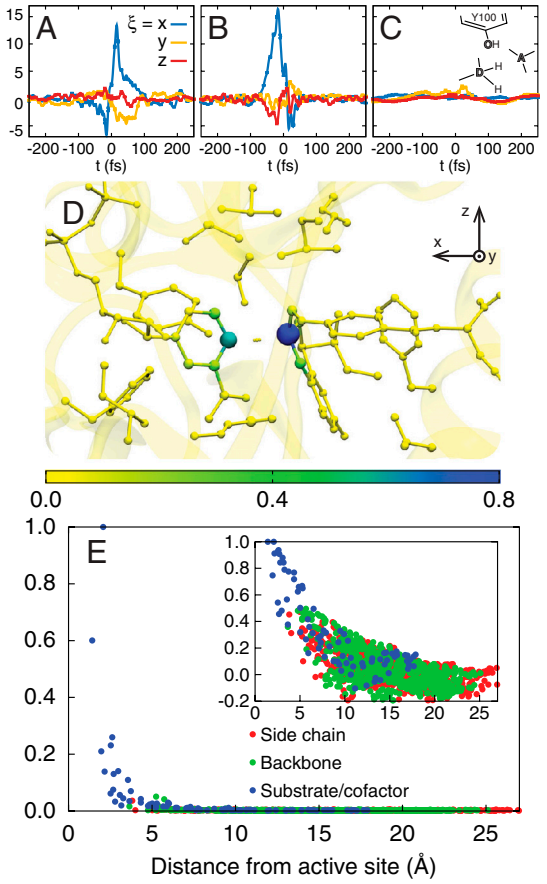

Fig. 3. The dynamical correlation measure $f_i^{\xi}(t)$, plotted for (*A*) the donor atom, (*B*) the acceptor atom, and (*C*) the side-chain O atom in the Y100 residue of the active site. (*D*) The size and color of atoms in the active-site region are scaled according to the integrated dynamical correlation measure, f_i. (*E*) (Main panel) The integrated dynamical correlation measure, f_i, as a function of the distance of atom i from the midpoint of the donor and acceptor atoms. (*Inset*) The statistical correlation measure, $\bar{c}_i$, is similarly presented. Atoms corresponding to the protein side chains, the protein backbone, and the substrate/cofactor regions are indicated by color. Values presented in part A are in units of nm/ps, and values in parts *D* and *E* are normalized to a maximum of unity. The estimated error in part *E* is smaller than the dot size.

The results presented here complement previous theoretical efforts to illuminate the role of protein motions in enzyme catalysis. For example, Neria and Karplus (32) used transmission coefficient calculations and constrained molecular dynamics (MD) trajectories to determine that the protein environment in triosephosphate isomerase (TIM) is essentially rigid (i.e., dynamically unresponsive) on the timescale of the intrinsic reaction dynamics; this finding is consistent with the lack of long-lengthscale dynamical correlations reported in the current study. Furthermore, Truhlar and coworkers (33, 34) and Karplus and Cui (35) both demonstrated that quasi-classical tunneling coefficients for hydrogen transfer evaluated at instantaneous enzyme configurations in the transition state region fluctuate significantly with donor-acceptor motions and other local active-site vibrations, which is likely consistent with the direct observation of short-lengthscale dynamical correlations reported here. However, by using quantized molecular dynamics to sample the ensemble of reactive trajectories in DHFR catalysis and to perform nonequilibrium ensemble averages that directly probe

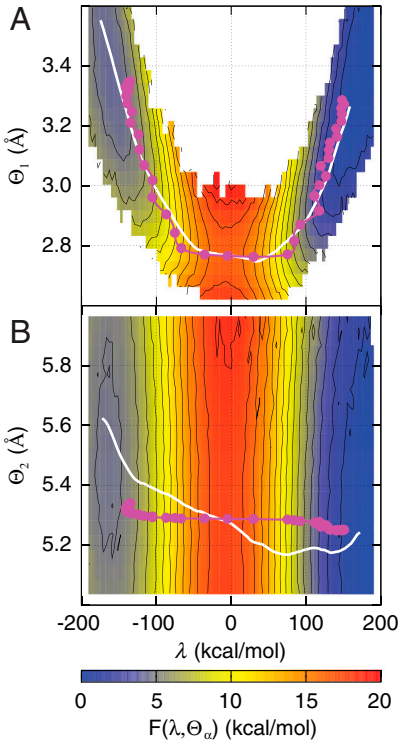

Fig. 4. Minimum free-energy pathways (*s*, white) and the mean pathway of the reactive trajectories (σ, magenta) overlay two-dimensional projections of the free-energy landscape, $F(\lambda,\Theta_\alpha)$. (*A*) $F(\lambda,\Theta_1)$, where Θ_1 is the distance between the hydride donor and acceptor atoms. (*B*) $F(\lambda,\Theta_2)$, where Θ_2 is the distance between side-chain atoms I14 C_δ and Y100 O in the active-site residues. The dots in the magenta curves indicate 5 fs increments in time. Nonzero slope in *s* and σ indicates statistical and dynamical correlations, respectively.

dynamical correlation, we provide a framework for strengthening and generalizing these earlier analyses. In particular, the current approach avoids transition state theory approximations by providing a rigorous statistical mechanical treatment of the ensemble of reactive trajectories, it allows for the natural characterization of lengthscales and timescales over which dynamical correlations persist, and it seamlessly incorporates dynamical effects due to both nuclear quantization and trajectory recrossing. We expect this approach to prove useful in future studies of dynamics in other enzymes, which will be necessary to confirm the generality of the conclusions drawn here.

Concluding Remarks

The physical picture that emerges from this analysis is one in which the intrinsic reaction involves a small, localized group of atoms that are dynamically uncoupled from motions in the surrounding protein environment. As in the canonical theories for electron and proton transfer in the condensed phase (36, 37), the strongly dissipative protein environment merely gates the fast dynamics in the active site. This view reconciles the observed kinetic effects of distal enzyme mutations (14, 15) with evidence for short-ranged dynamical correlations in the active site (9, 19, 20), and it supports a unifying theoretical perspective in which slow, thermal fluctuations in the protein modulate the instantaneous rate for the intrinsic reaction (4, 7, 17, 29, 30, 32, 33, 34, 35, 38, 39, 40, 41). Furthermore, the work presented here provides clear evidence against the proposed role of nonlocal, rate-promoting vibrational dynamics in the enzyme (8), and it reveals the strikingly short lengthscales over which nonequilibrium protein dynamics couples to the intrinsic reaction. The combination of quantized molecular dynamics methods (24) with trajectory sampling methods (28) provides a useful approach for characterizing mechanistic features of reactions involving significant quantum tunneling effects. These findings for the case of the DHFR enzyme, a good candidate for dynamical correlations because of its small size and strong network of statistical correlations, suggest that nonlocal dynamical correlations are neither a critical feature of enzyme catalysis nor an essential consideration in de novo enzyme design.

Materials and Methods

Calculation Details. All simulations are performed using a modified version of the Gromacs-4.0.7 molecular dynamics package (42). Further calculation details regarding the potential energy surface, the system initialization and equilibration protocol, free-energy sampling, and dividing surface sampling are provided in *SI Text*, Figs. S7–S9, and Table S1.

Ring Polymer Molecular Dynamics. The RPMD equations of motion (23) used to simulate the dynamics of DHFR are

$$\ddot{\mathbf{q}}_j = \frac{1}{nm_n}[k_n(\mathbf{q}_{j+1} + \mathbf{q}_{j-1} - 2\mathbf{q}_j) - \nabla_{\mathbf{q}_j} U(\mathbf{q}_j,\mathbf{Q}_1,\ldots,\mathbf{Q}_N)], \qquad j = 1,\ldots,n \quad [3]$$

$$\ddot{\mathbf{Q}}_k = -\frac{1}{nM_k}\sum_{j=1}^{n} \nabla_{\mathbf{Q}_k} U(\mathbf{q}_j,\mathbf{Q}_1,\ldots,\mathbf{Q}_N), \qquad k = 1,\ldots,N, \quad [4]$$

where $U(\mathbf{q}_j,\mathbf{Q}_1,\ldots,\mathbf{Q}_N)$ is the potential energy function for the system, $n = 32$ is the number of ring polymer beads used to quantize the hydride, $\mathbf{q}_j$ and m_n are the position and mass of the *j*th ring polymer bead, and $\mathbf{q}_0 = \mathbf{q}_n$. Similarly, *N* is the number of classical nuclei in the system, and $\mathbf{Q}_k$ and M_k are the position and mass of the *k*th classical atom, respectively. The interbead force constant is $k_n = m_H n^2/(\beta\hbar)^2$, where $m_H = 1.008$ amu is the mass of the hydride and $\beta = (k_B T)^{-1}$ is the reciprocal temperature; a temperature of $T = 300$ K is used throughout the study. For dynamical trajectories, RPMD prescribes that $m_n = m_H/n$.

Calculating the Statistical Correlation Functions, c_{ij}. In Fig. 3*A*, equilibrium ensemble averages are presented for the system in the reactant region, the dividing surface region, and the product region. These ensemble averages are strictly defined using

$$\langle A\rangle_{\lambda^*} = \int_{\lambda^*-\delta\lambda}^{\lambda^*+\delta\lambda} d\lambda' P(\lambda') \int d\mathbf{q}_1 \ldots \int d\mathbf{q}_n \int d\mathbf{Q}_1 \ldots \int d\mathbf{Q}_N \times \delta(\lambda' - \lambda(\mathbf{x}))A(\mathbf{q}_1,\ldots,\mathbf{q}_n,\mathbf{Q}_1,\ldots,\mathbf{Q}_N), \quad [5]$$

where $P(\lambda) = \exp(-\beta F(\lambda))/\int d\lambda' \exp(-\beta F(\lambda'))$, and $F(\lambda)$ is calculated using umbrella sampling, as described in *SI Text*. For the ensembles in the reactant, dividing surface, and product regions, we employ $\lambda^* = -181$ kcal/mol, −7 kcal/mol, and 169 kcal/mol, respectively, and $\delta\lambda = 2.5$ kcal/mol.

The Transition Path Ensemble. Reactive trajectories are generated through forward- and backward-integration of initial configurations drawn from the dividing surface ensemble with initial velocities drawn from the Maxwell–Boltzmann distribution. Reactive trajectories correspond to those for which forward- and backward-integrated half-trajectories terminate on opposite sides of the dividing surface. From the 10,500 half-trajectories that are initialized on the dividing surface (i.e., 5,250 possible reactive trajectories), over 3,000 reactive RPMD trajectories are obtained. For analysis purposes, the integration of these reactive trajectories was continued for a total length of 1 ps in both the forward and backward trajectories.

The reactive trajectories that are initialized from the equilibrium Boltzmann distribution on the dividing surface must be reweighted to obtain the unbiased ensemble of reactive trajectories (i.e., the transition path ensemble) (27, 28, 43). A weighting term is applied to each trajectory α, correctly accounting for the recrossing and for the fact that the trajectories are performed in the microcanonical ensemble (27),

$$w_\alpha = \left(\sum_{\text{intersections}\, i} |\dot{\lambda}_i|^{-1} \right)^{-1}, \qquad [6]$$

where the sum includes all instances in which trajectory α crosses the dividing surface, and $\dot{\lambda}_i$ is the velocity in the collective variable at crossing event *i*. We find that the relative statistical weight of all reactive trajectories that recross the dividing surface is 1.6%, emphasizing that recrossing does not play a large role in the current study.

ACKNOWLEDGMENTS. This work was supported by the National Science Foundation (NSF) CAREER Award (CHE-1057112) and computing resources at the National Energy Research Scientific Computing Center. Additionally, N.B. acknowledges an NSF graduate research fellowship, and T.F.M. acknowledges an Alfred P. Sloan Foundation fellowship.

1. Henzler-Wildman KA, et al. (2007) Intrinsic motions along an enzymatic reaction trajectory. *Nature* 450:838–844.
2. Boehr DD, McElheny D, Dyson HJ, Wright PE (2010) Millisecond timescale fluctuations in dihydrofolate reductase are exquisitely sensitive to the bound ligands. *Proc Natl Acad Sci USA* 107:1373–1378.
3. Cook PF, Cleland WW (2007) *Enzyme Kinetics and Mechanism* (Garland Science, New York).
4. Kamerlin SCL, Warshel A (2010) At the dawn of the 21st century: Is dynamics the missing link for understanding enzyme catalysis? *Proteins* 78:1339–1375.
5. Nashine VC, Hammes-Schiffer S, Benkovic SJ (2010) Coupled motions in enzyme catalysis. *Curr Opin Chem Biol* 14:644–651.
6. Garcia-Viloca M, Gao J, Karplus M, Truhlar DG (2004) How enzymes work: Analysis by modern rate theory and computer simulations. *Science* 303:186–195.
7. Schwartz SD, Schramm VL (2009) Enzymatic transition states and dynamic motion in barrier crossing. *Nat Chem Biol* 5:551–559.
8. Machleder SQ, Pineda JRET, Schwartz SD (2010) On the origin of the chemical barrier and tunneling in enzymes. *J Phys Org Chem* 23:690–695.
9. Masgrau L, et al. (2006) Atomic description of an enzyme reaction dominated by proton tunneling. *Science* 312:237–241.
10. Nagel ZD, Klinman JP (2009) A 21st century revisionist's view at a turning point in enzymology. *Nat Chem Biol* 5:543–550.
11. Agarwal PK, Billeter SR, Rajagopalan PTR, Benkovic SJ, Hammes-Schiffer S (2002) Network of coupled promoting motions in enzyme catalysis. *Proc Natl Acad Sci USA* 99:2794–2799.
12. Pang JY, Pu JZ, Gao JL, Truhlar DG, Allemann RK (2006) Hydride transfer reaction catalyzed by hyperthermophilic dihydrofolate reductase is dominated by quantum mechanical tunneling and is promoted by both inter- and intramonomeric correlated motions. *J Am Chem Soc* 128:8015–8023.
13. Rod TH, Radkiewicz JL, Brooks CL (2003) Correlated motion and the effect of distal mutations in dihydrofolate reductase. *Proc Natl Acad Sci USA* 100:6980–6985.
14. Wong KF, Selzer T, Benkovic SJ, Hammes-Schiffer S (2005) Impact of distal mutations on the network of coupled motions correlated to hydride transfer in dihydrofolate reductase. *Proc Natl Acad Sci USA* 102:6807–6812.
15. Wang L, Tharp S, Selzer T, Benkovic SJ, Kohen A (2006) Effects of a distal mutation on active site chemistry. *Biochemistry* 45:1383–1392.
16. Gira B, et al. (2011) A dynamic knockout reveals that conformational fluctuations influence the chemical step of enzyme catalysis. *Science* 332:234–238.
17. Benkovic SJ, Hammes-Schiffer S (2006) Enzyme motions inside and out. *Science* 312:208–209.
18. Truhlar DG (2010) Tunneling in enzymatic and nonenzymatic hydrogen transfer reactions. *J Phys Org Chem* 23:660–676.
19. Pudney CR, et al. (2009) Evidence to support the hypothesis that promoting vibrations enhance the rate of an enzyme catalyzed H-tunneling reaction. *J Am Chem Soc* 131:17072–17073.
20. Loveridge EJ, Tey LH, Allemann RK (2010) Solvent effects on catalysis by *Escherichia coli* dihydrofolate reductase. *J Am Chem Soc* 132:1137–1143.
21. Saen-Oon S, Quaytman-Machleder S, Schramm VL, Schwartz SD (2008) Atomic detail of chemical transformation at the transition state of an enzymatic reaction. *Proc Natl Acad Sci USA* 105:16543–16548.
22. Ball P (2004) By chance, or by design? *Nature* 431:396–397.
23. Craig IR, Manolopoulos DE (2004) Quantum statistics and classical mechanics: Real time correlation functions from ring polymer molecular dynamics. *J Chem Phys* 121:3368–3373.
24. Craig IR, Manolopoulos DE (2005) A refined ring polymer molecular dynamics theory of chemical reaction rates. *J Chem Phys* 123:034102.
25. Warshel A, Weiss RM (1980) An empirical valence bond approach for comparing reactions in solutions and in enzymes. *J Am Chem Soc* 102:6218–6226.
26. Liu HB, Warshel A (2007) Origin of the temperature dependence of isotope effects in enzymatic reactions: The case of dihydrofolate reductase. *J Phys Chem B* 111:7852–7861.
27. Hummer G (2004) From transition paths to transition states and rate coefficients. *J Chem Phys* 120:516–523.
28. Bolhuis PG, Chandler D, Dellago C, Geissler PL (2002) Transition path sampling: Throwing ropes over rough mountain passes, in the dark. *Annu Rev Phys Chem* 53:291–318.
29. Agarwal PK, Billeter SR, Hammes-Schiffer S (2002) Nuclear quantum effects and enzyme dynamics in dihydrofolate reductase catalysis. *J Phys Chem B* 106:3283–3293.
30. Garcia-Viloca M, Truhlar DG, Gao JL (2003) Reaction-path energetics and kinetics of the hydride transfer reaction catalyzed by dihydrofolate reductase. *Biochemistry* 42:13558–13575.
31. Rajagopalan PTR, Lutz S, Benkovic SJ (2002) Coupling interactions of distal residues enhance dihydrofolate reductase catalysis: Mutational effects on hydride transfer rates. *Biochemistry* 41:12618–12628.
32. Neria E, Karplus M (1997) Molecular dynamics of an enzyme reaction: Proton transfer in TIM. *Chem Phys Lett* 267:23–30.
33. Pu JZ, Ma SH, Gao JL, Truhlar DG (2005) Small temperature dependence of the kinetic isotope effect for the hydride transfer reaction catalyzed by Escherichia coli dihydrofolate reductase. *J Phys Chem B* 109:8551–8556.
34. Pu JZ, Gao JL, Truhlar DG (2006) Multidimensional tunneling, recrossing, and the transmission coefficient for enzymatic reactions. *Chem Rev* 106:3140–3169.
35. Cui Q, Karplus M (2002) Quantum mechanics/molecular mechanics studies of triosephosphate isomerase-catalyzed reactions: Effect of geometry and tunneling on proton-transfer rate constants. *J Am Chem Soc* 124:3093–3124.
36. Marcus RA, Sutin N (1985) Electron transfers in chemistry and biology. *Biochim Biophys Acta* 811:265–322.
37. Borgis D, Hynes JT (1996) Curve crossing formulation for proton transfer reactions in solution. *J Phys Chem* 100:1118–1128.
38. Knapp MJ, Klinman JP (2002) Environmentally coupled hydrogen tunneling: Linking catalysis to dynamics. *Eur J Biochem* 269:3113–3121.
39. Marcus RA (2006) Enzymatic catalysis and transfers in solution. i. theory and computations, a unified view. *J Chem Phys* 125:194504.
40. Kuznetsov AM, Ulstrup J (1999) Proton and hydrogen atom tunnelling in hydrolytic and redox enzyme catalysis. *Can J Chem* 77:1085–1096.
41. Szabo A, Shoup D, Northrup SH, Mccammon JA (1982) Stochastically gated diffusion-influenced reactions. *J Chem Phys* 77:4484–4493.
42. Hess B, Kutzner C, van der Spoel D, Lindahl E (2008) Gromacs 4: Algorithms for highly efficient, load-balanced, and scalable molecular simulation. *J Chem Theory Comput* 4:435–447.
43. E W, Vanden-Eijnden E (2006) Towards a theory of transition paths. *J Stat Phys* 123:503–523.

Supporting Information

Boekelheide et al. 10.1073/pnas.1106397108

SI Materials and Methods

Potential Energy Surface. The potential energy surface for the hydride transfer reaction in dihydrofolate reductase (DHFR) is described using the empirical valence bond (EVB) method (1, 2),

$$U(\mathbf{x}^{(j)}) = \frac{1}{2}(V_{\mathrm{r}}(\mathbf{x}^{(j)}) + V_{\mathrm{p}}(\mathbf{x}^{(j)})) - \frac{1}{2}\sqrt{(V_{\mathrm{r}}(\mathbf{x}^{(j)}) - V_{\mathrm{p}}(\mathbf{x}^{(j)}))^2 + 4V_{12}^2}. \qquad \textbf{[S1]}$$

As in the main text, the notation $\mathbf{x}^{(j)} \equiv (\mathbf{q}_j, \mathbf{Q}_1, \ldots, \mathbf{Q}_N)$ is used to indicate the position of ring-polymer bead j and the full set of classical nuclei. The terms $V_{\mathrm{r}}(\mathbf{x}^{(j)})$ and $V_{\mathrm{p}}(\mathbf{x}^{(j)})$ are the molecular mechanics potential energy functions for the system with the hydride covalently bonded to the donor and acceptor atoms, respectively. The constant $V_{12} = 30.6$ kcal/mol is fit to the experimental rate for the intrinsic reaction (3), and the product state potential $V_{\mathrm{p}}(\mathbf{x}^{(j)})$ includes a constant shift of $\Delta_{12} = +101.9$ kcal/mol to match the experimental driving force for the intrinsic reaction (3). The difference in the value for Δ_{12} used here versus in ref. 1 is due to different treatments of the atom-exclusions in the calculation of long-range electrostatic contributions.

Calculation of $V_{\mathrm{r}}(\mathbf{x}^{(j)})$ and $V_{\mathrm{p}}(\mathbf{x}^{(j)})$ is performed using a modified version of the GROMOS 43A1 united atom forcefield (4). These modifications, which again follow previous work (1, 5), are described in Fig. S7. A cutoff distance of 15 Å is applied to short-ranged nonbonding interactions, and electrostatic interactions beyond 9 Å are calculated using the particle mesh Ewald technique (6). The bond-lengths for all nontransferring hydrogen atoms in the system are constrained using the SHAKE algorithm (7).

To avoid sampling configurations of the enzyme that are not relevant to the intrinsic reaction, weak harmonic restraints were introduced between the simulated enzyme and the reference crystal structure (8). To avoid substrate dissociation during the long equilibrium sampling trajectories, weak harmonic restraints ($k = 0.15$ kcal mol^{-1} A^{-2}) are applied to the heavy atoms in the glutamate moiety of the substrate and to the α-carbons of the neighboring α-helix segment composed of residues 26 to 35; to prevent large-scale conformation rearrangements in DHFR (9), weak harmonic restraints ($k = 0.001$ kcal mol^{-1} A^{-2}) are applied to all other heavy atoms in the enzyme. Fig. S8 demonstrates that these restraints do not measurably affect the reactive trajectories used in our analysis of dynamical correlations.

Calculation Details. We initialize and equilibrate the system using the protocol described in ref. 1. The system is initialized from the DHFR crystal structure in the active configuration [Protein Data Bank (PDB) code 1RX2] (8). Crystallographic 2-mercaptoethanol and manganese ions are removed; crystallographic waters are not. The amine side chain of Q102 is rotated 180° to correctly coordinate the adenine moiety of the cofactor (10). To be consistent with the observed hydrogen bonding networks in the crystal structure, histidine residues 45, 124, and 149 are protonated at nitrogen ND1, histidine residues 114 and 141 are protonated at nitrogen NE2, and both DHFR cysteine residues are in their protonated form (11). The enzyme is explicitly solvated using 4,122 SPC/E rigid water molecules (11) in a truncated octahedral simulation cell with constant volume and periodic boundary conditions. The periodic image distance for the cell is 57.686 Å. Twelve Na^+ ions are included for charge neutrality. The full system includes $N = 14{,}080$ classical nuclei.

All ring-polymer molecular dynamics (RPMD) and classical molecular dynamics (MD) trajectories are numerically integrated using the leap-frog integrator implemented in Gromacs-4.0.7. The simultaneous positions and velocities for each integration time step in the trajectories are stored for analysis. Unless otherwise stated, the RPMD equations of motion are integrated using a time step of 0.025 fs and classical MD trajectories are integrated using a time step of 1 fs. The classical MD trajectories are used only for the initial equilibration of the system and for additional results presented here in *SI Text*; all data presented in the main text are obtained using the quantized RPMD trajectories. Throughout the text, standard error estimates are calculated from five block-averages of the data.

From the initial geometry of the crystal structure, the system is equilibrated on the reactant potential energy surface V_{r} using classical MD. In a series of three equilibration steps, MD trajectories of length 10 ps in time are performed with progressively weaker harmonic restraints between the heavy atom positions and the crystal structure; the restraint force constants for the three equilibration runs are 100, 50, and 25 kcal mol^{-1} A^{-2}, respectively, and the runs are performed at constant volume and temperature using the Berendsen thermostat with a coupling constant of 0.01 ps (12). After initial equilibration to the reactants basin, the system is equilibrated on the full potential energy surface (Eq. **S1**) for an additional 100 ps of classical MD. Finally, the ring-polymer representation for the quantized hydride was introduced at the geometry of the relaxed classical system and equilibrated for an additional 1 ps using RPMD with the Berendsen thermostat.

Free Energy Sampling. The free energy (FE) profile in Fig. 1 of the main text is calculated as a function of the collective variable $\lambda(\mathbf{x}^{\mathrm{c}}) \equiv V_{\mathrm{r}}(\mathbf{x}^{\mathrm{c}}) - V_{\mathrm{p}}(\mathbf{x}^{\mathrm{c}})$, where $\mathbf{x}^{\mathrm{c}} \equiv (\mathbf{q}^{\mathrm{c}}, \mathbf{Q}_1, \ldots, \mathbf{Q}_N)$, and $\mathbf{q}^{\mathrm{c}} = \sum_{j=1}^{n} \mathbf{q}_j / n$ is the ring-polymer centroid of mass $m_{\mathrm{c}} = n m_n$. The umbrella sampling method (13) is used to efficiently sample this collective variable between the reactant and product basins. Independent RPMD sampling trajectories are performed using biasing potentials of the form

$$\sum_{j=1}^{n}[V_{\mathrm{EVB}}(\mathbf{x}^{(j)})] + \frac{1}{2}k_l(\lambda(\mathbf{x}^{\mathrm{c}}) - \lambda_l)^2, \qquad l = 1, \ldots, 20, \qquad \textbf{[S2]}$$

where the $\{k_l\}$ and $\{\lambda_l\}$ are listed in Table S1.

For the RPMD trajectories used to sample the FE profile, a ring-polymer bead mass of $m_n = 12/n$ amu was used to diminish the separation of timescales for the motion of the ring-polymer and the rest of the system. Changing this parameter does not affect the ensemble of configurations that are sampled in the calculation of the FE profile; it merely allows for the sampling trajectories to be performed with a larger simulation time step (0.1 fs) than is used in the dynamical trajectories. Furthermore, unlike the RPMD dynamical trajectories in which the long-range electrostatic contributions are updated every time step, we use twin-ranged cutoffs (4) in the FE sampling trajectories such that nonbonding interactions beyond 9 Å are only updated every 5 fs. Sampling trajectories are performed at constant temperature using the velocity rescaling thermostat (14) with a relaxation time of 0.05 ps.

The sampling trajectories are initialized in order of increasing λ_l, as follows. The first sampling trajectory ($l = 1$) was initialized from the equilibrated system in the reactant basin. After 25 ps of simulation, the configuration from this first sampling trajectory was used to initialize the second sampling trajectory ($l = 2$). After 25 ps of simulation, the configuration from the second trajectory was used to initialize the third sampling trajectory ($l = 3$), and so on. A total simulation length of 6 ns is sampled for each value of l, and the weighted histogram analysis method (WHAM) (15) is used to calculate the unbiased FE profile $F(\lambda)$ from the set of sampling trajectories.

To improve the overlap of the trajectories in coordinates other than $\lambda(\mathbf{x}^c)$, we follow the swapping procedure described by Warshel and coworkers (16). Configurations are swapped between neighboring values of windows every 100 ps, and the first 25 ps after a swap are discarded. Comparing results obtained with and without the use of this swapping protocol, we found no significant difference in the calculated free energy profile (Fig. S9). Each sampling trajectory for the calculation of the FE profile without swapping was also of length 6 ns in time.

In addition to calculating the quantized FE profile using the RPMD sampling trajectories, we repeat the sampling protocol with classical MD trajectories to obtain the classical FE profile for the intrinsic reaction. Fig. S2*A* compares these two results; the results for the quantized system are identical to those from Fig. 1*B* in the main text.

For the calculation of equilibrium ensemble averages, the configurations of the enzyme are aligned to remove overall translational and orientational diffusion. As in previous studies (1), this is done using the following iterative protocol. In a first step, all configurations in the ensemble are aligned to the crystal structure, and the atom positions of the aligned structure are averaged. In a second step, all of the configurations in the ensemble are aligned to the average structure from the first step. In all cases, the RMSD between the average structures of subsequent iterations converged to within 10^{-7} Å in less than 20 iterations.

The Dividing Surface Ensemble. Boltzmann-weighted sampling on the reaction dividing surface ($\lambda(\mathbf{x}^c) = -4.8$ kcal/mol) is performed with constrained molecular dynamics using the SHAKE algorithm (7). The existing implementation of SHAKE in Gromacs-4.0.7 is modified to constrain both classical MD and RPMD with respect to the collective variable $\lambda(\mathbf{x}^c)$. To remove the hard-constraint bias from the ensemble of configurations that is sampled in the constrained dynamics (17, 18), each sampled configuration is weighted by $[H(\mathbf{x}^c)]^{-1/2}$, where

$$H(\mathbf{x}^c) = (m_c)^{-1}|\nabla_{\mathbf{q}^c}\lambda(\mathbf{x}^c)|^2 + \sum_{k=1}^{N} M_k^{-1}|\nabla_{\mathbf{Q}_k}\lambda(\mathbf{x}^c)|^2. \qquad \textbf{[S3]}$$

Seven long, independent RPMD trajectories are run with the dividing surface constraint. These constrained trajectories are initialized from configurations obtained in the umbrella sampling trajectories that are restrained to the dividing surface region using Eq. **S2**, and they are performed at constant temperature using the velocity rescaling thermostat (14) with a relaxation time of 0.05 ps. Following an initial equilibration of 25 ps, each of the constrained trajectories is run for 1 ns, and dividing surface configurations are sampled every 4 ps. As with the umbrella sampling trajectories, the constrained dynamics utilize a ring-polymer bead mass of $m_n = 12/n$ amu to enable a time step of 0.1 fs.

To eliminate the effects of overall translational and rotational diffusion from the analysis of the reactive trajectories, the phase-space points for the reactive trajectories are aligned at $t = 0$ (i.e., the point of initial release from the dividing surface). This is done exactly as in the calculation of equilibrium averages. Using the ensemble of configurations corresponding to reactive trajectories at $t = 0$, the rotation and translation for each particular trajectory is determined. This translation and rotation is applied to the configuration of each time step in the trajectory, and only the rotation is applied to the velocities at each time step in the trajectory.

Calculation of the Transmission Coefficient. Using a dividing surface of $\lambda(\mathbf{x}^c) = \lambda^{\ddagger}$, the time-dependent transmission coefficient for the reaction is (19–22)

$$\kappa(t) = \frac{\langle \dot{\lambda}(\mathbf{x}^c(0),\dot{\mathbf{x}}^c(0))\theta(\lambda(\mathbf{x}^c(t)) - \lambda^{\ddagger})\rangle_{\lambda^{\ddagger}}}{\langle \dot{\lambda}(\mathbf{x}^c(0),\dot{\mathbf{x}}^c(0))\theta(\dot{\lambda}(\mathbf{x}^c(0),\dot{\mathbf{x}}^c(0)))\rangle_{\lambda^{\ddagger}}}, \qquad \textbf{[S4]}$$

where $\langle \ldots \rangle_{\lambda^{\ddagger}}$ denotes the Boltzmann-weighted distribution of configurations on the dividing surface, and $\theta(x)$ is the Heaviside function. The transmission coefficient is evaluated by initializing RPMD trajectories from configurations $(\mathbf{x}^c(0))$ on the dividing surface with velocities $(\dot{\mathbf{x}}^c(0))$ drawn from the Maxwell–Boltzmann distribution. These initial configurations are then correlated with the configurations $(\mathbf{x}^c(t))$ reached by the unconstrained RPMD trajectories after evolving the dynamics for time t.

In the current study, each sampled configuration on the dividing surface is used to generate three unconstrained RPMD trajectories that are evolved both forward and backward in time for 100 fs, such that 10,500 half-trajectories are released from the dividing surface. The initial velocities for each trajectory are drawn independently; these time-zero velocities, the time-zero positions, and the corresponding time-zero forces at the initial positions are used to initialize the leap-frog integrator.

In addition to calculating the transmission coefficient for the quantized hydride transfer using RPMD, we repeat the protocol with classical MD trajectories to obtain the classical transmission coefficient. Fig. S2*B* compares these two results; the results for the quantized system are identical to those from Fig. 1*C* in the main text.

Additional Measures of Dynamical Correlations. To confirm that Fig. 2 in the main text, which considers only heavy atom positions, did not neglect important dynamical correlations, we include the corresponding plots with all atoms for the enzyme included (Fig. S3). To examine the robustness of our conclusions about dynamical correlations in the system, we present various alternative measures of dynamical correlations in Figs. S4–S6. Fig. S4 presents alternative methods for analyzing the dynamical correlation measure $d_{ij}(t)$. In Fig. S5, we present a measure of dynamical correlations that are nonlocal in time,

$$d_{ij}^{\Delta t}(t) = \frac{\langle \mathbf{v}_i(t)\cdot\mathbf{v}_j(t+\Delta t)\rangle_t}{(\langle|\mathbf{v}_i(t)|^2\rangle_t\langle|\mathbf{v}_j(t+\Delta t)|^2\rangle_t)^{1/2}} - \frac{\langle \mathbf{v}_i(t)\cdot\mathbf{v}_j(t+\Delta t)\rangle}{(\langle|\mathbf{v}_i|^2\rangle\langle|\mathbf{v}_j|^2\rangle)^{1/2}}, \qquad \textbf{[S5]}$$

where $\langle \ldots \rangle_t$ and $\langle \ldots \rangle$ are defined as in the main text. In Fig. S6, we present a measure of dynamical correlations between perpendicular components of the velocity,

$$d_{ij}^{\perp,\xi_1,\xi_2}(t) = \frac{D_{ij}^{\perp,\xi_1,\xi_2}(t)}{(D_{ii}^{\perp,\xi_1,\xi_1}(t)D_{jj}^{\perp,\xi_2,\xi_2}(t))^{1/2}}, \qquad \textbf{[S6]}$$

where

$$D_{ij}^{\perp,\xi_1,\xi_2}(t) = \langle(\bar{v}_i^{\xi_1}(t) - \langle\bar{v}_i^{\xi_1}\rangle)(\bar{v}_j^{\xi_2}(t) - \langle\bar{v}_j^{\xi_2}\rangle)\rangle_t, \qquad \textbf{[S7]}$$

and where $\bar{\mathbf{v}}_i = (\bar{v}_i^1, \bar{v}_i^2, \bar{v}_i^3)$ is the absolute velocity vector in Cartesian coordinates. As for the measures presented in the main text, dynamical correlations are found to be localized in the substrate and cofactor regions, with only weak signatures in the protein residues surrounding the active site.

1. Agarwal PK, Billeter SR, Hammes-Schiffer S (2002) Nuclear quantum effects and enzyme dynamics in dihydrofolate reductase catalysis. *J Phys Chem B* 106:3283–3293.
2. Warshel A, Weiss RM (1980) An empirical valence bond approach for comparing reactions in solutions and in enzymes. *J Am Chem Soc* 102:6218–6226.
3. Fierke CA, Johnson KA, Benkovic SJ (1987) Construction and evaluation of the kinetic scheme associated with dihydrofolate-reductase from *Escherichia coli*. *Biochemistry* 26:4085–4092.
4. van Gunsteren WF, et al. (1996)*Biomolecular Simulation: The GROMOS96 Manual and User Guide* (Hochschuleverlag AG an der ETH Zürich, Zürich, Switzerland).
5. Wong KF, Watney JB, Hammes-Schiffer S (2004) Analysis of electrostatics and correlated motions for hydride transfer in dihydrofolate reductase. *J Phys Chem B* 108:12231–12241.
6. Darden T, York D, Pedersen L (1993) Particle mesh Ewald: An N·log(N) method for Ewald sums in large systems *J Chem Phys* 98:10089–10092.
7. Ryckaert JP, Ciccotti G, Berendsen HJC (1977) Numerical-integration of cartesian equations of motion of a system with constraints: Molecular-dynamics of *n*-alkanes. *J Comput Phys* 23:327–341.
8. Sawaya MR, Kraut J (1997) Loop and subdomain movements in the mechanism of *Escherichia coli* dihydrofolate reductase: Crystallographic evidence. *Biochemistry* 36:586–603.
9. Arora K, Brooks CL (2009) Functionally important conformations of the Met20 loop in dihydrofolate reductase are populated by rapid thermal fluctuations. *J Am Chem Soc* 131:5642–5647.
10. Khavrutskii IV, Price DJ, Lee J, Brooks CL (2007) Conformational change of the methionine 20 loop of *Escherichia coli* dihydrofolate reductase modulates pK_a of the bound dihydrofolate. *Protein Sci* 16:1087–1100.
11. Berendsen HJC, Grigera JR, Straatsma TP (1987) The missing term in effective pair potentials. *J Phys Chem* 91:6269–6271.
12. Berendsen HJC, Postma JPM, Vangunsteren WF, Dinola A, Haak JR (1984) Molecular-dynamics with coupling to an external bath. *J Chem Phys* 81:3684–3690.
13. Torrie GM, Valleau JP (1977) Nonphysical sampling distributions in Monte Carlo free-energy estimation: Umbrella sampling. *J Comput Phys* 23:187–199.
14. Bussi G, Donadio D, Parrinello M (2007) Canonical sampling through velocity rescaling. *J Chem Phys* 126:014101.
15. Kumar S, Bouzida D, Swendsen RH, Kollman PA, Rosenberg JM (1992) The weighted histogram analysis method for free-energy calculations on biomolecules. I. The method. *J Comput Chem* 13:1011–1021.
16. Liu HB, Warshel A (2007) Origin of the temperature dependence of isotope effects in enzymatic reactions: The case of dihydrofolate reductase. *J Phys Chem B* 111:7852–7861.
17. Zichi DA, Ciccotti G, Hynes JT, Ferrario M (1989) Molecular-dynamics simulation of electron-transfer reactions in solution. *J Phys Chem* 93:6261–6265.
18. Frenkel D, Smit B (2002) *Understanding Molecular Simulation: From Algorithms to Applications*, Computational Science Series (Academic, San Diego), 2nd Ed.
19. Bennett CH (1977) *Algorithms for Chemical Computations*, ACS Symposium Series (American Chemical Society, Washington, DC) Vol. 46, pp 63–97.
20. Chandler D (1978) Statistical-mechanics of isomerization dynamics in liquids and transition-state approximation. *J Chem Phys* 68:2959–2970.
21. Craig IR, Manolopoulos DE (2005) A refined ring polymer molecular dynamics theory of chemical reaction rates. *J Chem Phys* 123:034102.
22. Craig IR, Manolopoulos DE (2005) Chemical reaction rates from ring-polymer molecular dynamics. *J Chem Phys* 122:084106.

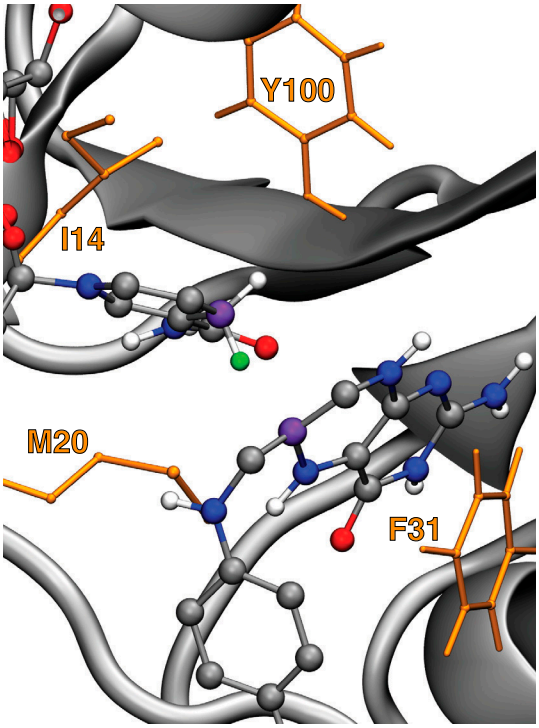

Fig. S1. The active site region of the DHFR enzyme, with the transferring hydride (green) in the reactant state, the donor and acceptor carbon atoms in purple, and relevant protein residues in gold.

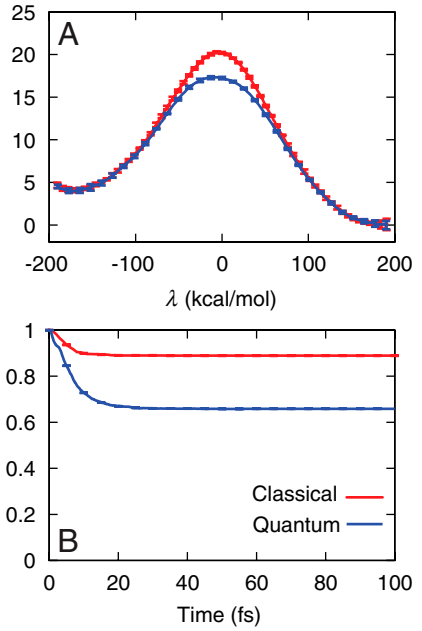

Fig. S2. (*A*) The quantized and classical free energy profiles for the reaction. (*B*) The quantized and classical time-dependent transmission coefficient corresponding to the dividing surface at $\lambda(\mathbf{x}) = -4.8$ kcal/mol.

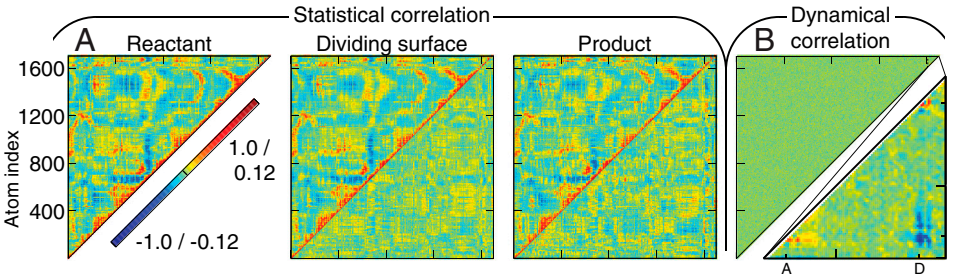

Fig. S3. (*A*) (Upper triangles) The covariance c_{ij} among position fluctuations in DHFR, plotted for the reactant, dividing surface, and product regions. All atoms are indexed according to PDB ID code 1RX2. (Lower triangles) The difference with respect to the plot for the reactant basin. (*B*) (Upper triangle) The integrated dynamical correlation measure d_{ij}, indexed as in (*A*). (Lower triangle) The substrate and cofactor regions are enlarged. Dynamical correlations between atom-pairs that share a holonomic constraint are excluded from part B. Comparison of the current figure (which includes all atoms) with Fig. 2 in the main text (which includes only heavy atoms) leaves the conclusions from the main text unchanged.

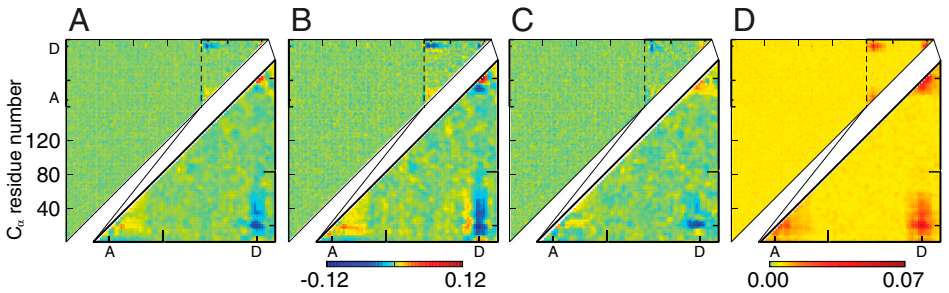

Fig. S4. Alternative measures of the dynamical correlation. (*A*) The integrated dynamical correlation measure $d_{ij} = \int_{-\tau}^{\tau} dt d_{ij}(t)$, reproduced from Fig. 2*E* of the main text. (*B*) Including only the forward-integrated time, $\int_{0}^{\tau} dt d_{ij}(t)$. (*C*) Including only the backward-integrated time, $d_{ij} = \int_{-\tau}^{0} dt d_{ij}(t)$. (*D*) Including the integrated absolute value, $\int_{-\tau}^{\tau} dt |d_{ij}(t)|$. In all cases, $\tau = 100$ fs.

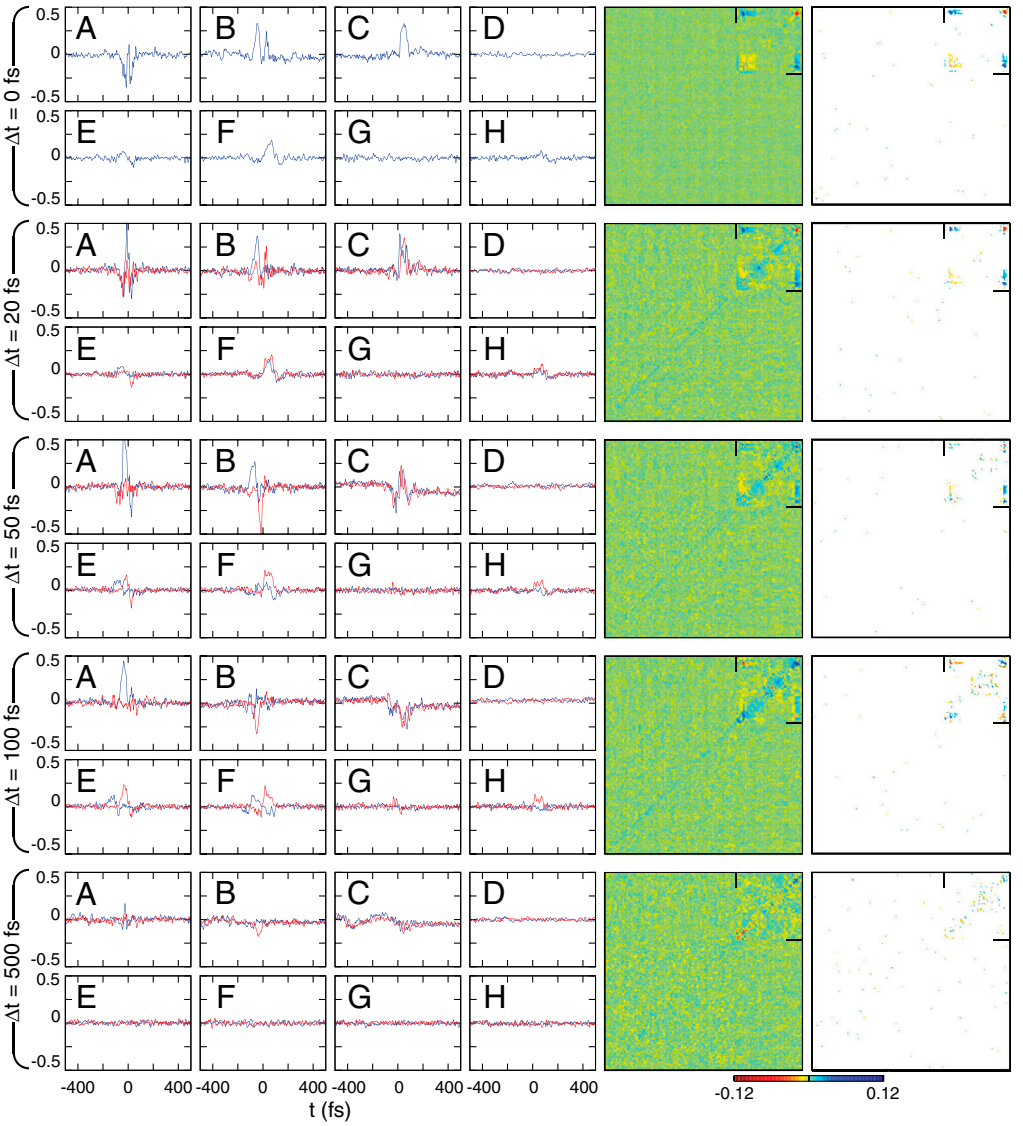

Fig. S5. (*A–H*) The measure of temporally nonlocal dynamical correlations, $d_{ij}^{\Delta t}(t)$, plotted at various separation times Δt and for various atom pairs, including (*A*) the donor and acceptor atom pair, (*B*) the substrate-based C_7 and the acceptor atom pair, (*C*) the cofactor-based CN_4 and donor atom pair, (*D*) the active site-based protein atoms that define the distance Θ_2 in Fig. 4*B* (*E*) the active-site-based backbone I4 O and the acceptor atom pair, (*F*) the active-site-based backbone I4 O and the donor atom pair, (*G*) the active-site-based backbone G95 C_α and the acceptor atom pair, and (*H*) the active-site-based backbone G95 C_α and the donor atom pair. Two curves (red and blue) are plotted, because $d_{ij}^{\Delta t}(t)$ is not symmetric with respect to atom indices *i* and *j* for nonzero Δt. At right, the integrated measure $d_{ij}^{\Delta t} = \int_{-\tau}^{\tau} dt d_{ij}^{\Delta t}(t)$ for each lag time, plotted as a function of the protein α-carbon atoms and the heavy atoms of the substrate and cofactor, as in Fig. 2*E* in the main text. In all cases, $\tau = 100$ fs. At far right, the same integrated measure is replotted, only displaying data points for which the magnitude of the integrated measure exceeds twice the estimated standard error.

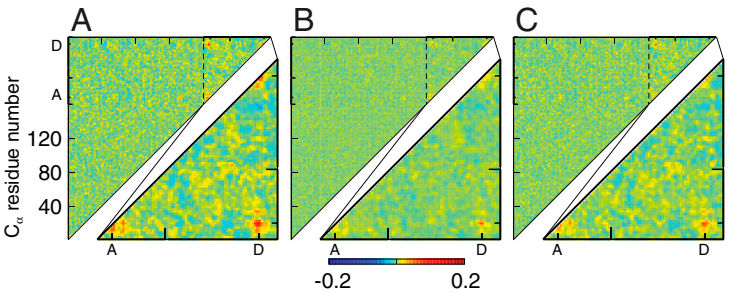

Fig. S6. The measure of dynamical correlations between perpendicular components of the velocity, $d_{ij}^{\perp,\xi_1,\xi_2}(t)$. (*A*) The integrated measure $d_{ij}^{\perp} = \sum_{\xi_1,\xi_2=1}^{3} \int_{-\tau}^{\tau} dt d_{ij}^{\perp,\xi_1,\xi_2}(t)$ that includes all components. (*B*) The integrated measure $d_{ij}^{\perp} = \sum_{\xi}^{3} \int_{-\tau}^{\tau} dt d_{ij}^{\perp,\xi,\xi}(t)$ that includes only diagonal components. (*C*) The integrated measure $d_{ij}^{\perp} = \sum_{\xi_1 \neq \xi_2=1}^{3} \int_{-\tau}^{\tau} dt d_{ij}^{\perp,\xi_1,\xi_2}(t)$ that includes only off-diagonal components. In all cases, $\tau = 100$ fs, and the integrated measures are plotted as a function of the protein α-carbon atoms and the heavy atoms of the substrate and cofactor, as in Fig. 2*E* in the main text.

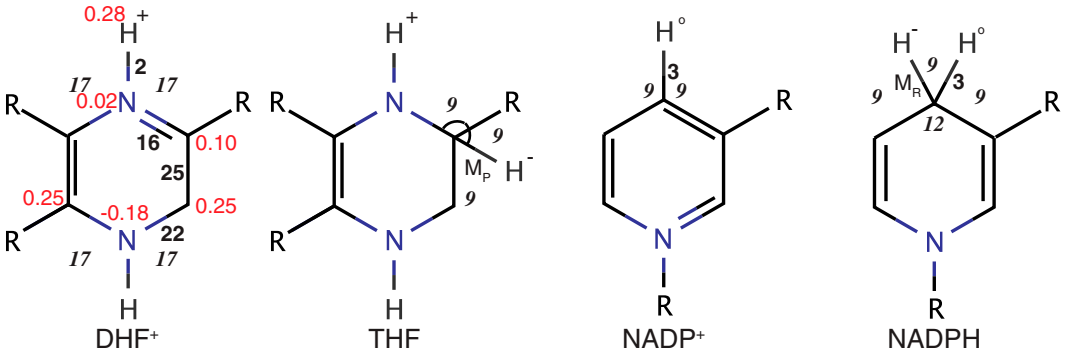

Fig. S7. Modifications to the GROMOS 43A1 united atom forcefield only involve the DHF^+, THF, $NADP^+$, and NADPH species. The resulting potential energy surface is as close as possible to that used in earlier studies of statistical correlation in DHFR hydride transfer catalysis (1). Only parameters that differ from the GROMOS forcefield are indicated; parameters shown for DHF^+ differ with respect to those for 7,8-dihydrofolate (DHF). In red, the atomic charges for DHF^+ are shown. In black, the bond-type (bold) and angle-type (italics) indices for the GROMOS forcefield are shown. Explicit representations are used for the transferring hydride (H^-) in the THF and NADPH species, the pro-*S* hydrogen atom (H°) in the NADPH and $NADP^+$ species, and the proton (H^+) attached to the nearest neighbor of the donor carbon. Firstly, we describe the treatment of H^-. The transferring hydride interacts with the donor and acceptor carbons via Morse potentials M_R and M_P, respectively (1). Following GROMOS convention, nonbonding interactions are excluded between H^- and its first-, second-, and third-nearest neighbors, defined in terms of bonding connectivity. Additionally, nonbonding interactions between H^- and the H°, donor, and acceptor atoms are excluded, regardless of the local bonding environment of the H^- atom. Secondly, we describe the treatment of H°. The bond length for H° is constrained to a fixed value of 1.09 Å , and planarity of H° with respect to the nicotinamide ring in $NADP^+$ is enforced using the planar improper dihedral angle potential in GROMOS. As for the hydride, nonbonding interactions are excluded between H° and its first-, second-, and third-nearest neighbors. Thirdly, we describe the treatment of H^+. Nonbonding interactions are excluded between H^+ and its first- and second-nearest neighbors; third-nearest neighbor nonbonding interactions are treated through using a 1–4 potential. For the LJ interactions involving these explicit hydrogen atoms, H^+ is treated using the parameters for a charged hydrogen, and both H° and H^- are treated using the parameters for a hydrogen bound to a carbon. For the LJ interactions involving the donor and acceptor, these atoms are treated using the parameters for a bare carbon atom.

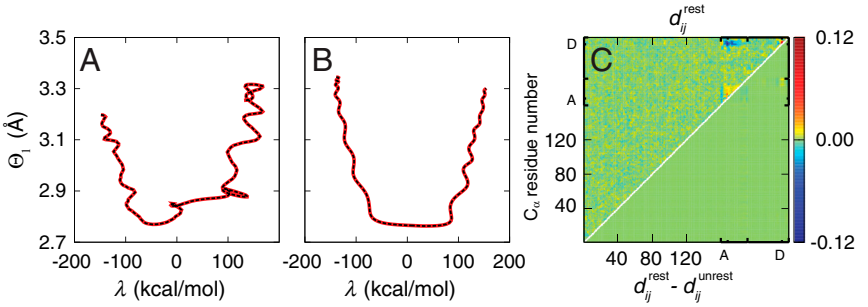

Fig. S8. Tests of the degree to which the weak harmonic restraints impact the dynamics of the reactive trajectories. (*A*) Comparison of two trajectories that are initialized from the same positions and velocities on the dividing surface, which are calculated with (red) and without (black) the weak restraints. Trajectories are evolved for a total of 200 fs and are viewed in the plane of the donor-acceptor distance ($\Theta_1(\mathbf{x}^c)$) and the reaction progress variable ($\lambda(\mathbf{x}^c)$). (*B*) In red, the mean pathway from the ensemble of 750 reactive trajectories, $\sigma = (\langle\lambda(\mathbf{x}^c)\rangle_t, \langle\Theta_1(\mathbf{x}^c)\rangle_t)$, calculated for trajectories obtained with the weak restraints. In black, the mean pathway from the ensemble of 750 trajectories that are initialized from the same phase-space points but which do not include the weak restraints. (*C*) (Upper triangle) The dynamical correlation measure d_{ij}^{rest}, calculated from an ensemble of 750 reactive trajectories using the weak harmonic restraints; this quantity is identical to the that reported in Fig. 2*E* of the main text, except that fewer trajectories are used here. (Lower triangle) The difference between d_{ij}^{rest} and d_{ij}^{unrest}, which is calculated from the ensemble of 750 trajectories that are initialized from the same phase-space points but which do not include the weak restraints. For all three tests, the impact of the weak restraints on the dynamics of the reactive trajectories is undetectable.

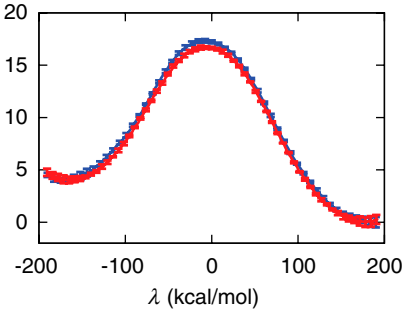

Fig. S9. Free energy profiles obtained with (red) and without (blue) swapping of configurations from neighboring 6 ns sampling trajectories in the WHAM calculation.

Table S1. The umbrella sampling parameters $\{\lambda_I\}$ and $\{k_I\}$ in units of kcal/mol and mol/kcal, respectively

I	λ_I	k_I
1	−188.7	0.002
2	−154.0	0.002
3	−120.0	0.002
4	−87.1	0.002
5	−57.4	0.004
6	−56.1	0.002
7	−35.8	0.004
8	−18.3	0.004
9	−17.8	0.008
10	−6.4	0.008
11	1.4	0.004
12	1.5	0.008
13	4.3	0.006
14	14.2	0.004
15	23.3	0.002
16	34.2	0.004
17	57.9	0.002
18	95.8	0.002
19	135.7	0.002
20	170.0	0.000